ORIGINAL PAPER

Novel active–passive compensator–supercapacitor modeling for low-voltage ride-through capability in DFIG-based wind turbines

M. Kenan Döşoğlu[1] · **Osman Özkaraca**[2] · **Uğur Güvenç**[1]

Abstract

Low-voltage ride-through is important for the operation stability of the system in balanced- and unbalanced-grid-fault-connected doubly fed induction generator-based wind turbines. In this study, a new LVRT capability approach was developed using positive–negative sequences and natural and forcing components in DFIG. Besides, supercapacitor modeling is enhanced depending on the voltage–capacity relation. Rotor electro-motor force is developed to improve low-voltage ride-through capability against not only symmetrical but also asymmetrical faults of DFIG. The performances of the DFIG with and without the novel active–passive compensator–supercapacitor were compared. Novel active–passive compensator–supercapacitor modeling in DFIG was carried out in MATLAB/SIMULINK environment. A comparison of the system behaviors was made between three-phase faults, two-phase faults and a phase–ground fault with and without a novel active–passive compensator–supercapacitor modeling. Parameters for the DFIG including terminal voltage, angular speed, electrical torque variations and d–q axis rotor–stator current variations, in addition to a 34.5 kV bus voltage, were investigated. It was found that the system became stable in a short time and oscillations were damped using novel active–passive compensator–supercapacitor modeling and rotor EMF.

Keywords Low-voltage ride-through · Novel active–passive compensator–supercapacitor modeling · DFIG-based wind turbine

List of symbols

K	Gain
P	Active power (W)
Q	Reactive power (W)
V	Voltage (V)
i	Current (A)
L	Inductance (H)
w	Angular speed (m/s)
DC	Direct current (A)

Abbreviations

LVRT	Low-voltage ride-through
DFIG	Doubly fed induction generator
EMF	Electro-motor force
NAPC	Novel active–passive compensator
TSO	Transmission system operators
WT	Wind turbine
FACTS	Flexible AC transmission system
STATCOM	Static synchronous compensator
ESS	Energy storage system

✉ M. Kenan Döşoğlu
  kenandosoglu@duzce.edu.tr

1   Department of Electrical-Electronics Engineering, Technology Faculty, Düzce University, 81620 Düzce, Turkey

2   Department of Information Systems Engineering, Technology Faculty, Muğla Sıtkı Koçman University, 48000 Muğla, Turkey

1 Introduction

As wind power penetration levels are increased in the power systems of many parts of the world, certain technical requirements regarding connecting large wind farms need to be clarified. This need is required by the grid codes of transmission system operators (TSO), which mainly concern large wind farms that are connected to transmission systems. These requirements typically concern large wind farms connected to the transmission system, rather than smaller power stations connected to the distribution network. The new grid codes indicate that wind farms need to contribute to the power system control just like conventional power stations and that the grid emphasizes the wind farm behavior under abnormal operating conditions. Grid code requirements have recently been a major force in the development of wind farm

technology. Grid code requirements that allow the wind farm to operate with the grid according to certain criteria are used in countries such as Germany, Spain, Ireland, Canada, England, Denmark, Scotland, UK, Sweden, Italy, USA and Turkey. Countries applying grid code requirements do comprehensive and detailed comparisons for the effects of voltage drops according to different scenarios. As a result of these comparisons, up-to-date innovations are made for grid requirements in wind power plants and generators [1]. One economical option for wind farms is doubly fed induction generator (DFIG). This method presents a decrease in the required costs and occurring power loss [2–4]. As its stator is directly connected to the grid, the DFIG is sensitive to grid disturbances and faults and makes it hard to meet the low-voltage ride-through (LVRT) requirements. Therefore, in the literature, different methods have been used for LVRT capability in DFIG. Rotor-side converter circuit of the DFIG has suffered from grid faults such as overcurrents and overvoltage. In order to overcome these problems, a new flux modeling and virtual resistance unit for LVRT capability are developed [5, 6]. On the other hand, series of grid-side converters and hybrid current control models are used to protect against the overcurrent grid-side converter of the DFIG [7, 8]. These models result in decreases in the adverse effects of balanced and unbalanced voltage dips. Different sliding mode control methods are used for the uncertainties of parameters in grid faults. Generally, robust fractional-order sliding mode and second-order sliding mode are used as different sliding models for LVRT capability in DFIG [9, 10]. To ensure that the real power flow maintains the fast-dynamic performance of the DFIG, different DC link models are developed [11, 12]. These DC link models are important to support LVRT capability during faults. In order to ensure the validity and feasibility of the DFIG for LVRT capability, $d–q$ coupled and $d–q$ flux control models are preferred. To meet the grid code requirements, these developed models are provided within a short-time stability of the system during balanced and unbalanced voltage dips [13, 14]. In order to improve the LVRT capability in DFIG during balanced faults, feedforward current control has been used. Because of this current control, the transient rotor currents and crowbar interruptions that occur during balanced faults are decreased. In addition, torque ripples are reduced by using inner current loop and power loop with feedforward current control [15–17]. Frequency response is not provided because of the decoupling between the power and the grid frequency during voltage dip in rotor-side and grid-side converters of DFIG. Therefore, coordinated frequency regulations such as primary and secondary frequency have been used [18, 19]. Dynamic voltage resistor is one of the most commonly used devices in rotor-side converters and grid-side converters of DFIG for LVRT capability. Series of damping and braking resistors are also provided for the control of DFIG during

various voltage dips [20, 21]. The use of the crowbar protection system is important for LVRT capability in terms of true activation–deactivation time constants in DFIG. Without the damping and braking resistors and the crowbar unit, a crowbarless control strategy is developed for control in DFIG [22]. All control strategies of DFIG during balanced and unbalanced faults are used for LVRT capability including flexible AC transmission system (FACTS) devices. Generally, static synchronous compensator (STATCOM) has been provided for reactive power and voltage controls [23, 24]. Energy storage system (ESS) is used to enhance the LVRT capability in DFIG not only during normal conditions but also during transient conditions. ESS devices such as supercapacitors and batteries are provided to control active power generation of the DC link voltage with charge–discharge time [25, 26]. New LVRT capability methods are developed using active and passive compensators in DFIG. Active and reactive compensator models called new LVRT capability methods are successful in more reliable operations of rotor-side converters and grid-side converters in DFIG [27, 28].

In Refs. [21, 27, 29–32], active–passive compensator, demagnetization control, stator damping resistor unit, rotor current control, positive–negative sequence dynamic modeling, ESS with supercapacitor and static synchronous compensator (STATCOM)-supercapacitor modeling in the DFIG-based wind turbine were developed for the LVRT capability in a DFIG, because constant flux linkage causes the stator flux not to follow the stator voltage instantaneous chances in Refs. [21, 27, 29–32]. Therefore, in this study, a new model was developed for LVRT capability in DFIG. Novel active–passive compensator (NAPC) and rotor electro-motor force (EMF) were enhanced using stator–rotor EMF models, positive sequence model and negative sequence model, and natural flux model was promoted using flux forcing for symmetrical and unsymmetrical faults. Moreover, the supercapacitor circuit was mathematically modeled in the grid-side converter circuit of a DFIG. DFIG terminal voltage, 34.5 kV bus voltage, DFIG angular speed, DFIG electrical torque and DFIG $d–q$ axis stator current variations were investigated. As a result of this study, it was found that the NAPC method yielded the efficient results for LVRT. Through this method, it is aimed to eliminate the negative conditions that may occur in the system. In the following segments, we examine modeling for DFIG, discuss the development of active–passive compensator modeling, investigate the modeling of supercapacitor for DFIG and show the simulation results of a 2.3-MW DFIG to confirm the efficacy of the suggested modeling for LVRT. The last and sixth segment is the conclusion.

2 Materials and methods

2.1 Modeling of the DFIG

As can be seen in Fig. 1, the circuit model of a DFIG is made up of a grid-side converter, a rotor-side converter and a crowbar unit.

Rotor-side and grid-side converters, shown in Eqs. 1–14, are the key components for the voltage and angle control and the active and reactive power control of DFIG in both steady-state and voltage dips.

$$\frac{dx_1}{dt} = P_{ref} + P_s \tag{1}$$

$$i_{qr\_ref} = K_{p1}(P_{ref} + P_s) + K_{i1}x_1 \tag{2}$$

$$\frac{dx_2}{dt} = i_{qr\_ref} - i_{qr} = K_{p1}(P_{ref} + P_s) + K_{i1}x_1 - i_{qr} \tag{3}$$

$$\frac{dx_3}{dt} = v_{s\_ref} - v_s \tag{4}$$

$$i_{dr\_ref} = K_{p3}(v_{s\_ref} - v_s) + K_{i3}x_3 \tag{5}$$

$$\frac{dx_4}{dt} = i_{dr\_ref} - i_{dr} = K_{p3}(v_{s\_ref} - v_s) + K_{i3}x_3 - i_{dr} \tag{6}$$

$$v_{qr} = K_{p2}(K_{p1}\Delta P + K_{i1}x_1 - i_{qr}) + K_{i2}x_2 + sw_sL_mi_{ds} + sw_sL_{rr}i_{qr} \tag{7}$$

$$v_{dr} = K_{p2}(K_{p3}\Delta v + K_{i3}x_3 - i_{dr}) + K_{i2}x_4 - sw_sL_mi_{qs} - sw_sL_{rr}i_{dr} \tag{8}$$

$$\frac{dx_5}{dt} = V_{dc\_ref} - V_{dc} \tag{9}$$

$$i_{dgrid\_ref} = -K_{pdgrid}\Delta v_{dc} + K_{1dgrid}x_5 \tag{10}$$

$$\frac{dx_6}{dt} = i_{dgrid\_ref} - i_{dgrid} = -K_{pdgrid}\Delta v_{dc} + K_{1dgrid}x_5 - i_{dgrid} \tag{11}$$

$$\frac{dx_7}{dt} = i_{qgrid\_ref} - i_{qgrid} \tag{12}$$

$$\Delta v_{dgrid} = K_{pgrid}\frac{dx_6}{dt} + K_{igrid}x_6 = K_{pgrid} \\ \times (-K_{pdgrid}\Delta v_{dc} + K_{1dgrid}x_5 - i_{dgrid}) + K_{1grid}x_6 \tag{13}$$

$$\Delta v_{qgrid} = K_{pgrid}\frac{dx_7}{dt} + K_{igrid}x_7 = K_{pgrid}(i_{qgrid\_ref} - i_{qgrid}) + K_{1grid}x_7. \tag{14}$$

x_1, x_2, x_3, x_4 are the control equations of the rotor-side converter, respectively; K_{p1} and K_{i1} are the proportional and integrating gains of the power regulator, respectively; K_{p2} and K_{i2} are the proportional and integrating gains of the rotor-side converter current regulator, respectively; K_{p3} and K_{i3} are the proportional and integrating gains of the grid voltage regulator, respectively; i_{dr_ref} and i_{qr_ref} are the current control references for the d and q axis components of the rotor-side converter, respectively; v_s and v_{s_ref} are the specified terminal voltage and specified reference voltage, respectively; P_s and P_{ref} are the active power control references, respectively; s is the slip, w_s is the angular speed of the stator, L_m is the magnetic inductance, L_{rr} is the sum of the rotor inductance and the magnetic inductance; Δv and ΔP are voltage and active power variation values, respectively; v_{dr} and v_{qr} are the d and q axis voltages of the rotor, respectively; i_{ds}, i_{dr}, i_{qs}, i_{qr} are the d and q axis currents of the stator and rotor, respectively; x_5, x_6, x_7 are the control equations of the grid-side converter, respectively; K_{pdgrid} and K_{idgrid} are the proportional and integrating gains of the DC bus voltage regulator, respectively; K_{pgrid} and K_{igrid} are the proportional and integrating gains of the grid-side converter current regulator, respectively; V_{dc} and V_{dc_ref} are the DC link voltage and voltage reference of the DC link, respectively; i_{dgrid} and i_{dgrid_ref} are the d axis component of the grid-side converter current and the control reference for the q axis component of the grid-side converter current, respectively;

Fig. 1 DFIG circuit model
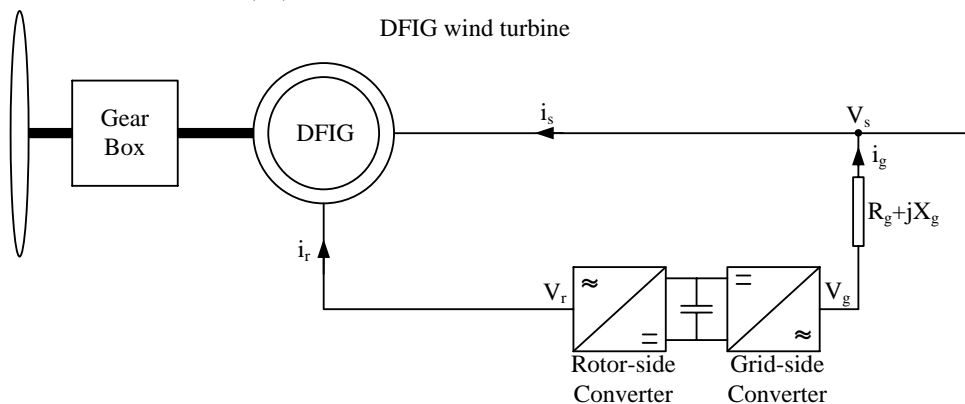
i_{qgrid} and i_{qgrid_ref} are the q axis component of the grid-side converter current and the control reference for the q axis component of the grid-side converter current, respectively; Δv_{dgrid} and Δv_{qgrid} are the d and q axis of the grid-side converter voltage variation values, respectively; and Δv_{dc} is the DC link voltage variation value [33].

The calculations for the active and reactive powers used by the DFIG from the rotor current and grid voltage can be found in Eqs. 15 and 16.

$$P_s = V_{grid} \frac{L_m}{L_s} i_{dqr} \tag{15}$$

$$Q_s = V_{grid} \frac{L_m}{L_s} i_{dqr} - \frac{V_{grid}^2}{w_s L_s}. \tag{16}$$

P_s stands for the active power of the DFIG, Q_s stands for the reactive power, and V_{grid} stands for the grid voltage. Taking into account the variables of the generator in the d–q synchronous reference frame, the model of the DFIG is explained in five equations. Equations 17–20 show the stator and rotor windings voltage and include the flux equations.

$$v_{dqs} = R_s i_{dqs} \pm jw_s \lambda_{dqs} + \frac{d}{dt} \lambda_{dqs} \tag{17}$$

$$v_{dqr} = R_r i_{dqr} \mp jsw_s \lambda_{qr} + \frac{d}{dt} \lambda_{dqr} \tag{18}$$

$$\lambda_{dqs} = (L_s + L_m) i_{dqs} + L_m i_{dqr} \tag{19}$$

$$\lambda_{dqr} = (L_r + L_m) i_{dqr} + L_m i_{dqs}. \tag{20}$$

v_{ds}, v_{dr}, v_{qs}, v_{qr} are the d and q axis voltages of the stator and rotor, respectively; i_{ds}, i_{dr}, i_{qs}, i_{qr} are the d and q axis currents of the stator and rotor, respectively; λ_{ds}, λ_{qs}, λ_{dr}, λ_{qr} are the d and q axis fluxes of the stator and rotor, respectively; w_s is the angular speed of the stator; s is the slip; R_s and R_r are the stator and rotor resistances, respectively; L_s and L_r are the stator and rotor inductances, respectively; and L_m is the magnetic inductance [34–36].

2.2 Enhancement of active–passive compensator modeling in DFIG

We can use positive–negative sequence models in stator voltage at the time of faults to improve the new NAPC modeling in DFIG. Equation 21 shows the d–q axis voltage equation [37, 38].

$$v_{dqs} = V_{s1} e^{jw_s t} + V_{s2} e^{-jw_s t}. \tag{21}$$

w_s stands for the angular speed of the reference frame, and V_{s1} and V_{s2} stand for the positive–negative sequence voltages. Equation 22 shows the steady-state components of the stator flux in the grid faults, disregarding the small voltage drop of the stator resistance.

$$\lambda_{ss} = \lambda_{s1} + \lambda_{s2} = \frac{V_{s1}}{jw_s} e^{jw_s t} + \frac{V_{s1}}{-jw_s} e^{-jw_s t}. \tag{22}$$

ss is the steady-state component. As the flux is a state variable, it has to constantly differ between the initial state and the steady state. Equations 23 and 24 show the stator and rotor steady-state components and the natural- and enhanced-forcing flux components.

$$\lambda_{dqs} = \lambda_{sdq1} + \lambda_{sdq2} + \lambda_{sdqn} + \lambda_{dqnf}$$
$$= \frac{V_{s1}}{jw_s} e^{jw_s t} + \frac{V_{s1}}{-jw_s} e^{-jw_s t} + (\lambda_{sn0} + \lambda_{nf0}) e^{-t/\tau_s} \tag{23}$$

$$\lambda_{dqr} = \frac{V_{s1}}{jw_s} e^{js \cdot w_s t} + \frac{V_{s1}}{-jw_s} e^{-j(2-s)w_s t} + (\lambda_{sn0} + \lambda_{nf0}) e^{-t/\tau_s} e^{jwt}. \tag{24}$$

The rotor back EMF voltage component is triggered by the stator flux. The voltage triggered by the EMF is:

$$E_r = \frac{L_m}{L_s} \left[s V_{s1} e^{js \cdot w_s t} + (2-s) V_{s2} e^{-j(2-s)w_s t} + (1-s) K e^{-(1/t_s + jwt)} \right]. \tag{25}$$

K stands for the simplification coefficient. Equation 23 shows the positive and negative sequence and the natural–forcing components of the stator flux. In normal conditions, the first segment of Eq. 25 is led by the stator flux positive sequence. Although not significant, the segment is a part of the slip frequency. The first segment stays low in transient conditions $(2-s)$, and the latter parts become high $(1-S)$. The DFIG cannot provide support power and voltage to the system because the lack of power support to the grid results in an increase in the rotor speed along with excessive rotor currents and oscillations in the stator. This increase leads to electromagnetic torque oscillations, possibly causing the extermination of the RSC. This lack of support power and grid voltage in DFIG is provided through the active compensator, which is achieved by controlling the rotor-side and grid-side converters, hence decreasing the stator flux oscillations and providing reactive power for the grid to support the grid voltage recovery. Equations 26 and 27 show the d–q synchronous stator voltage and current equations.

$$v_{dqs} = R_s i_{dqs} \pm jw_s \lambda_{dqs} + \frac{d}{dt} \lambda_{dqs} \tag{26}$$

$$i_{dqs} = \frac{\lambda_{dqs}}{L_s} - \frac{L_m}{L_s} i_{dqr}. \tag{27}$$

If we substitute Eq. 27 into 26, the stator flux n the d–q synchronous reference frame in terms of stator voltage and rotor current becomes:

$$\frac{\lambda_{dqs}}{dt} = v_{dqs} - jw_s\lambda_{dqs} - \frac{R_s}{L_s}\lambda_{dqs} + \frac{R_sL_m}{L_s}i_{dqr}. \tag{28}$$

If we separate Eq. 28 into positive and negative sequences and natural and forcing components, we get:

$$\frac{\lambda_{dqs1}}{dt} = v_{dqs1} - jw_s\lambda_{dqs1} - \frac{R_s}{L_s}\lambda_{dqs1} + \frac{R_sL_m}{L_s}i_{dqr1} \tag{29}$$

$$\frac{\lambda_{dqs2}}{dt} = v_{dqs2} - jw_s\lambda_{dqs2} - \frac{R_s}{L_s}\lambda_{dqs2} + \frac{R_sL_m}{L_s}i_{dqr2} \tag{30}$$

$$\frac{\lambda_{dqsn}}{dt} = v_{dqsn} - jw_s\lambda_{dqsn} - \frac{R_s}{L_s}\lambda_{dqsn} + \frac{R_sL_m}{L_s}i_{dqrn} \tag{31}$$

$$\frac{\lambda_{dqsf}}{dt} = v_{dqsf} - jw_s\lambda_{dqsf} - \frac{R_s}{L_s}\lambda_{dqsf} + \frac{R_sL_m}{L_s}i_{dqrf}. \tag{32}$$

The variations in the stator flux according to the d–q synchronous reference frame turn out to be zero, because its positive sequence component rotates at the angular speed of ω_s under grid voltage dips. Setting Eq. 30 to zero helps decrease the oscillations of the negative sequence component of the stator flux under grid voltage dips, and setting Eqs. 31 and 32 to zero helps do the same for the natural and forcing components. The following equations show the negative sequence component and the natural and forcing components of the rotor current reference.

$$i^*_{dqr2} = -\frac{L_s}{R_sL_m}\left(-v_{dqs2} - jw_s\lambda_{dqs2} - \frac{R_s}{L_s}\lambda_{dqs2}\right) \tag{33}$$

$$i^*_{dqrn} = -\frac{L_s}{R_sL_m}\left(-jw_s\lambda_{dqsn} - \frac{R_s}{L_s}\lambda_{dqsn}\right) \tag{34}$$

$$i^*_{dqrf} = -\frac{L_s}{R_sL_m}\left(-jw_s\lambda_{dqsf} - \frac{R_s}{L_s}\lambda_{dqsf}\right) \tag{35}$$

The rotor current references in the synchronous reference frame in Eqs. 33 and 35 are:

$$i^*_{dqr2} + i^*_{dqrn} + i^*_{dqrf}$$
$$= -\frac{L_s}{R_sL_m}\left(v_{dqs2} - jw_s(\lambda_{dqs2} + \lambda_{dqsn} + \lambda_{dqsf}) - \frac{R_s}{L_s}(\lambda_{dqs2} + \lambda_{dqsn} + \lambda_{dqsf})\right) \tag{36}$$

Separating Eq. 36 into d–q axis components, we get:

$$i^*_{dr2} + i^*_{drn} + i^*_{drf}$$
$$= -\frac{L_s}{R_sL_m}\left(v_{ds2} + w_s(\lambda_{ds2} + \lambda_{dsn} + \lambda_{dqsf}) - \frac{R_s}{L_s}(\lambda_{ds2} + \lambda_{dsn} + \lambda_{dsf})\right) \tag{37}$$

$$i^*_{qr2} + i^*_{qrn} + i^*_{qrf}$$
$$= -\frac{L_s}{R_sL_m}\left(v_{qs2} - w_s(\lambda_{qs2} + \lambda_{qsn} + \lambda_{qsf}) - \frac{R_s}{L_s}(\lambda_{qs2} + \lambda_{qsn} + \lambda_{qsf})\right). \tag{38}$$

As shown in Eqs. 36–38, the needed rotor current references for the suggested scheme under heavy voltage dips are quite high, as the stator resistance is low. We used a stator damping resistor to decrease the needed rotor current references under the rotor-side converter maximum current limits, as it cannot supply currents that high because of its limited capacity.

$$v_{dqr} = R_r i_{dqr} + \sigma L_r\frac{di_{dqr}}{dt} + \frac{L_m}{L_s}\frac{d}{dt}\lambda_{dqs} \tag{39}$$

The stator flux derivative is:

$$\frac{\lambda_{dqs}}{dt} = v_{dqs} - jw_r\lambda_{dqs} - \frac{R_s\lambda_{dqs}}{L_s} + \frac{R_sL_mi_{dqr}}{L_s} \tag{40}$$

If we substitute Eq. 40 into 39, the rotor voltage becomes:

$$v_{dqr} = \left(R_r + \frac{L_m^2}{L_s^2}R_s\right)i_{dqr} + \sigma L_r\frac{di_{dqr}}{dt} + \frac{L_m}{L_s}\times\left(v_{dqs} - jw_s - \frac{R_s\lambda_{dqs}}{L_s}\right) \tag{41}$$

So, the voltage in the rotor rotational reference frame is:

$$v_{dqr} = R_r'i_{dqr} + \sigma L_r\frac{di_{dqr}}{dt} + \frac{L_m}{L_s}\times\left(v_{dqs} - jw_s - \frac{R_s\lambda_{dqs}}{L_s}\right) \tag{42}$$

The rotor transient resistance becomes:

$$R_r' = R_r + \frac{L_m^2}{L_s^2}R_s. \tag{43}$$

The stator resistance and the rotor transient resistance in Eq. 43 are directly proportional. Thus, the stator flux damping is expedited, as the rotor inrush currents are decreased.

2.3 Supercapacitor modeling in DFIG

Implementing a supercapacitor to a DC bus, the grid-side converter works as an active power source. Connecting ESS to a DC bus can be done either directly or via an interface. Use of a supercapacitor modeling in DFIG is given in Fig. 2.

Here, the connection was done via a 2-quadrant DC/DC converter. As ESS sets generator output power with

Fig. 2 Connection of the supercapacitor in the DC/DC converter circuit
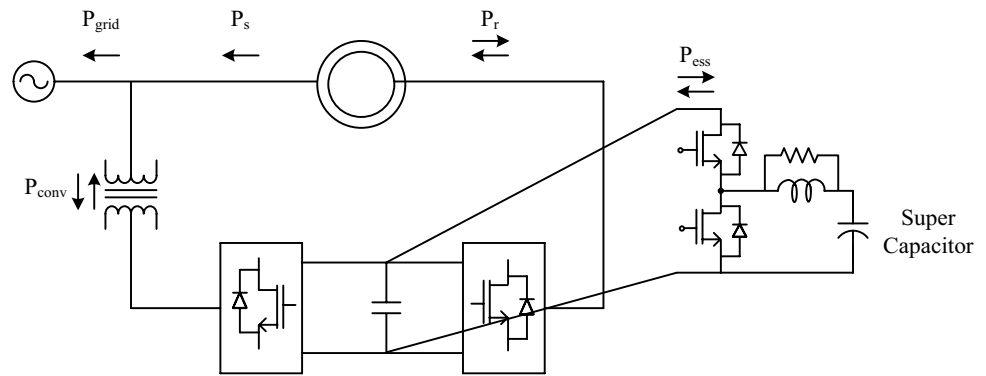
the grid-side converter, DC voltage is set with DC chopper circuit. Following this topology, ESS is able to set DC bus voltage between a minimum of 0 and a maximum of 100%, surpassing which causes ESS saturation. Based on the time, the power needs to be divided into specific ratios; as the grid in ESS provides 20% of the power, the input moment of DFIG provides 80%. Equations 44 and 45 show stored energy, and 46 shows the capacitance.

$$E_{ESS} = 0.2 P_{nominal} t \tag{44}$$

$$E_{ESS} = \frac{1}{2} C_{supercapacitor}(V_{max}^2 - V_{min}^2) \tag{45}$$

$$C_{supercapacitor} = \frac{0.4 P_{nominal} t}{(V_{max}^2 - V_{min}^2)}. \tag{46}$$

E_{ESS} stands for the quantity of stored energy, $P_{nominal}$ stands for the nominal power, t for the active circuit time of the supercapacitor, $C_{supercapacitor}$ for the capacity of the supercapacitor, and V_{max} and V_{min} for the maximum and minimum voltages. Energy storage power rating can alternate between systems. One very important and cost-effective method is to select small power wind farms for large power systems. Hence, fewer ESS devices can be used, which would make it easier to set the output power through ESS by DFIG.

Power rating in energy storage may vary according to the system. Using fewer ESS devices by choosing small power wind farms for large power systems is crucial in terms of the cost. Using smaller wind farms facilitates the adjustment of output power by DFIG through ESS [32, 39].

Grid-side converter circuit is used to regulate the output power of DFIG, which provides the reactive power required by the system, along with the bus voltage of DC. For the reference value, the reactive power reference and voltage of the AC bus are selected. To achieve maximum reactive power compensation values, we calculated the converter limits. Figure 3 shows the modeling of DC/DC converter and supercapacitor.

After taking the difference between DC voltage and DC voltage reference into proportional integral control, we calculate the signal's proportional limit value based on the maximum and minimum parameters. The output of the limit value is calculated by the d-axis reference current. A supercapacitor circuit is formed of four resistance banks and two capacitor banks. The supercapacitor that is used to regulate the capacity also regulates the system based on voltage. We find the capacity value by applying interpolation to the capacity–voltage curve.

3 Proposed LVRT modeling in DFIG

If we reduce the oscillations of the positive–negative sequences, we also reduce the natural and forcing components of the stator flux, the peak values and oscillations of the rotor voltage, the stator and rotor currents, electromagnetic torque, active and reactive powers in the stator, active power in the rotor and the DC link voltage. In our study, the DC link capacitor, the mechanical parts and the RSC have all remained safely under grid voltage dips. Figure 4 shows the modeling of the NAPC-supercapacitor in DFIG that are improved to meet the LVRT requirements.

Fault detection was used in the LVRT model as intended in Fig. 4. The difference between the measured voltage and the reference voltage was transferred to active power and reactive power. The values obtained in fault detection were summed up with the negative sequence component and the natural and forcing components of the rotor current reference values. The general rotor d–q axis reference currents of the system were calculated with the obtained value. After obtaining the general rotor d–q axis reference current and the d–q axis rotor currents, the d–q axis was converted to the abc axis. The obtained abc conversion goes directly into the rotor-side converter circuit. DC link reference value was calculated with the DC link voltage, and the minimum and maximum current values of the grid-side converter circuit were calculated with reactive power and reference reactive
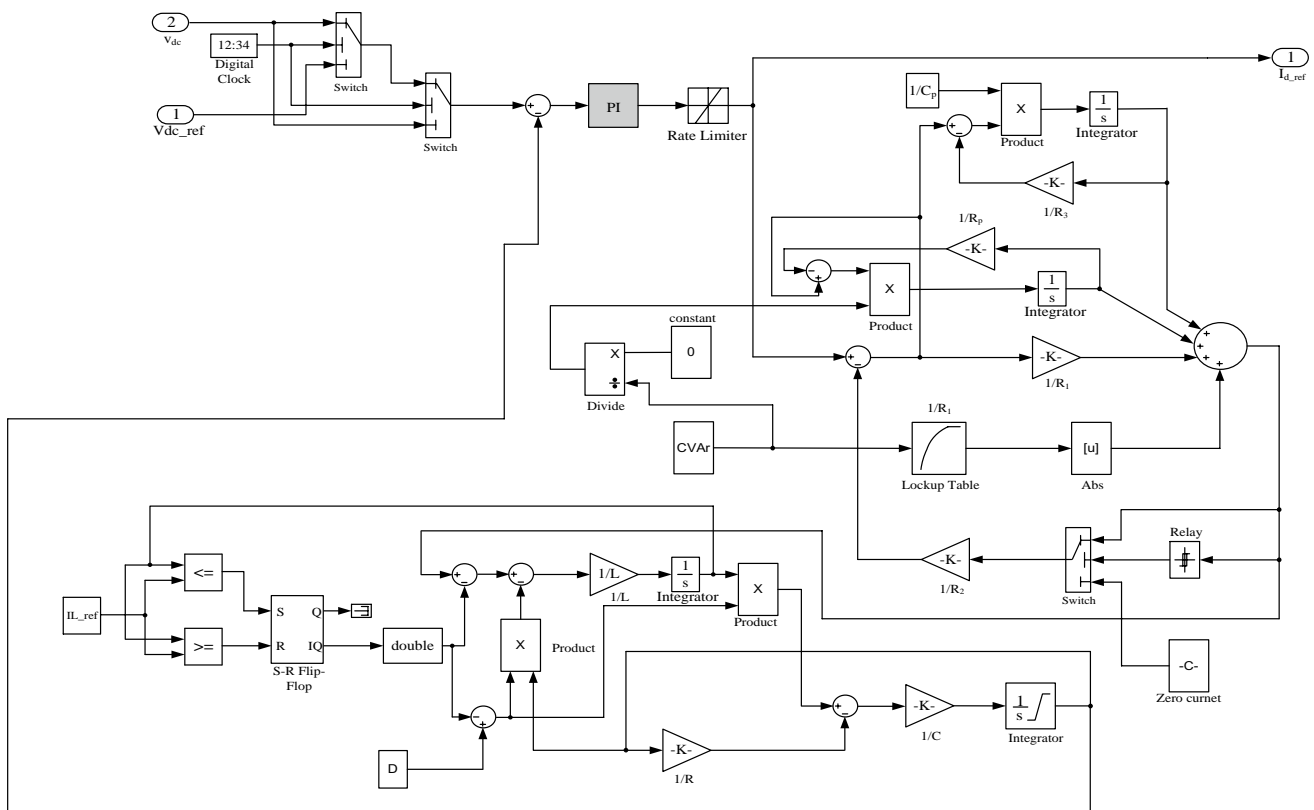
Fig. 3 Supercapacitor modeling

power values. These calculated values were transferred to the GSC circuit by performing *d–q/abc* conversion.

To form the active and reactive powers in the stator, we defined the rotor current references under normal grid conditions. But to obtain a better LVRT capability, the rotor current references of the suggested plan were put on top of to the power controller outputs in grid voltage dip conditions. To provide reactive power for the grid, the reactive power reference in the stator was defined based on the most recent grid code requirements. Figure 4 shows the block diagram used to evaluate the positive and negative sequences and the natural and forcing components of the stator voltage and flux for accurate calculations of the rotor current references. In our study, we utilized a method based on an algorithm decomposing the positive and negative sequences and the natural and forcing components to determine grid voltage dips [6], as this determination plays a significant role in quickly switching between normal and LVRT controls. This method can be seen in Fig. 4. V_{s1} stands for the positive sequence component amplitude dip used to determine the occurrence of voltage dip. V_s stands for the normal stator voltage amplitude. Occurrence of a voltage dip is presumed whenever $V_{s1} \leq 0.9V_s$. In this case, the controls are switched to the suggested LVRT instantly. If $V_{s1} > 0.9V_s$, however, the suggested LVRT control is

turned off. The grid-side converter control is mainly used to provide a stable DC link voltage and secondarily to adjust the injected reactive power to the grid. As mentioned before, DFIG converters have a capacity limit. In normal operations, keeping the grid-side converter reactive power reference at zero reduces the current and the losses in the converters, and in voltage dip occurrence, providing reactive power helps meet the most recent grid code requirements. In case of grid voltage dips, the highest feasible reactive power is needed to be injected into the grid and that is what the grid-side converter is used for. For the DFIG, the effect on the local bus should be limited while helping the voltage recover to the nominal range following the isolation of the fault by the system protection. Maintenance of the connection is needed during the fault. To achieve this, we provide a constant reactive power or constantly regulate the system voltage. In addition, the generator provides energy following the clearance of the disturbance, and one does not have to restart the system to do this. Supercapacitor energy storage helps all of these processes. It limits the acceleration of the machine and maintains the DC voltage in disturbances.
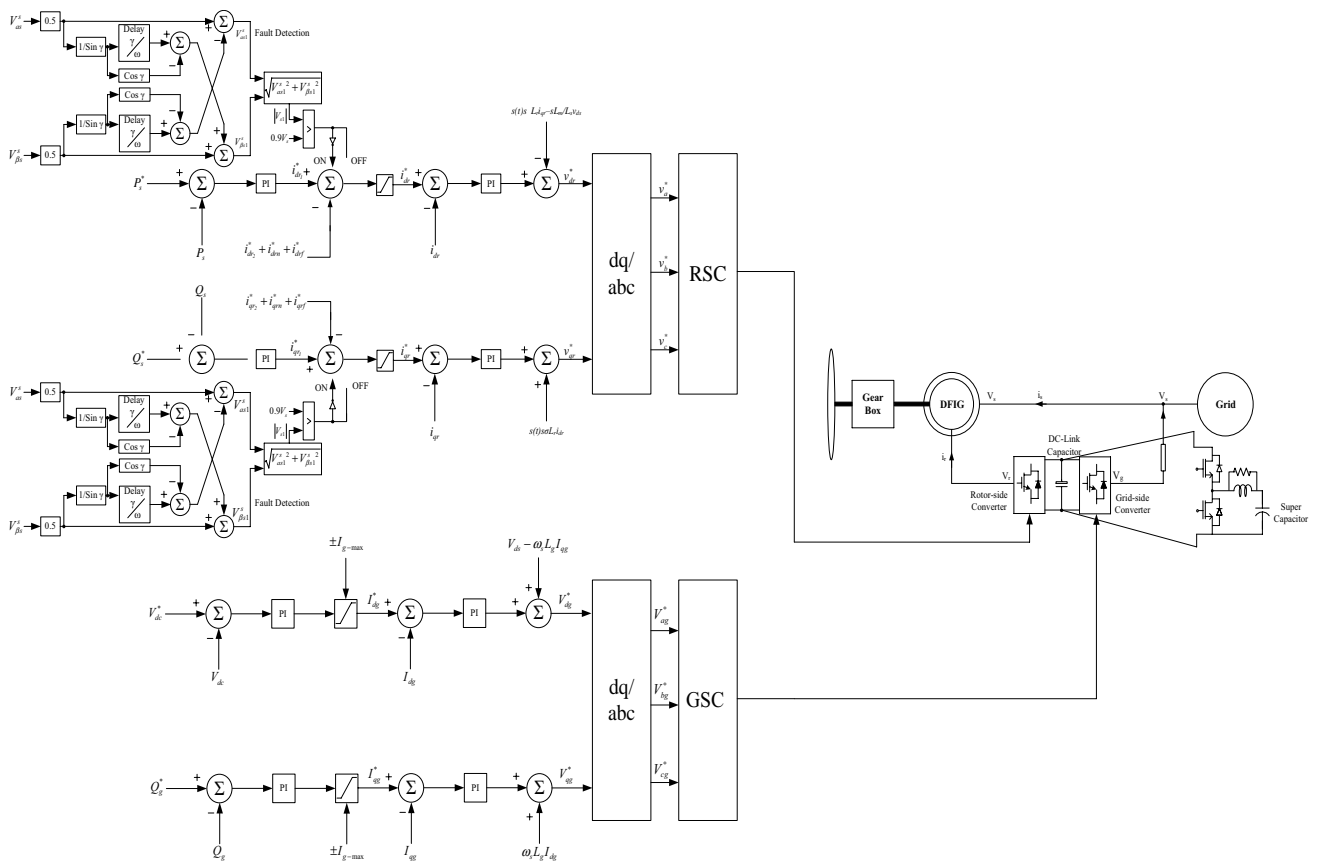
Fig. 4 Enhanced LVRT capability modeling

4 Simulation study

Figure 5 shows the wind power system, utilized to observe the transient behavior during the interaction of the 2.3-MW DFIG-based wind turbine and grid.

Here, we used the NAPC modeling of the DFIG model, along with positive and negative sequences and natural

and forcing components. We connected the wind power plant to a 34.5-kV system via two transformers that were 50 MVA, 154 Y/34.5 kV Y and 2.6 MVA, 34.5 Δ/0.69 kV Y. The length of the connection was 10 km, and the wind speed was stable at an 8 m/s. We chose the 34.5-kV grid-side short circuit power as 2500 MVA. The X/R rate was determined at 6. The generator parameters for the DFIG were as follows: stator and rotor resistances at 0.00706 Ω
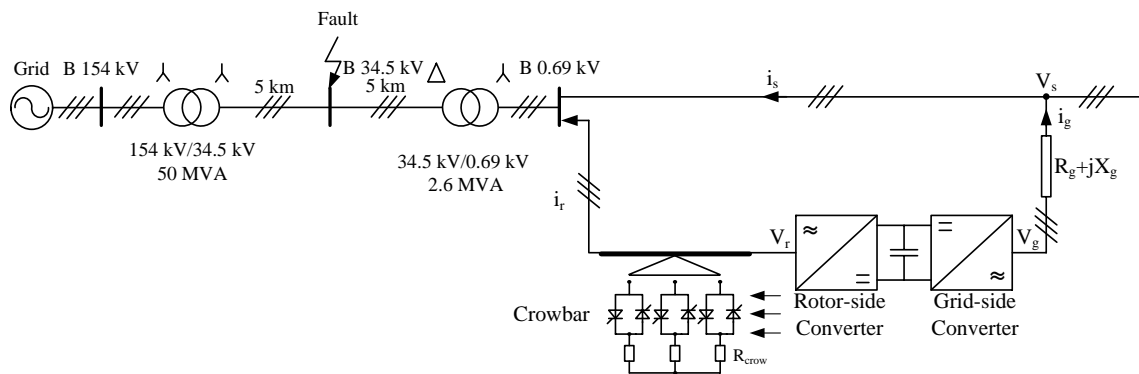

Fig. 5 Test system

and 0.005 Ω, respectively; stator, rotor and magnetization inductances were at 0.171, 0.156 and 2.9 Henry, respectively. In the simulation, fault and snubber resistances were 0.001 and 10,000 Ω. Depending on grid code requirement in Turkey, in this study, three-phase fault, two-phase fault and a phase–ground fault times were determined as 150 ms [40].

Observing the time representation of the system and the approximation decomposition levels for the inrush current collision defect, we see that the fault voltage drop may be ejected. A clear fault was detected at 0.1 s.

5 Simulation results

We identified the effect of the positive and negative sequences and the natural and forcing components on the system values at three transient events. We observed the first one to be a three-phase fault, which occurred in B34.5 kV bus in 0.55–0.7 s. Figure 6 shows the variations in 34.5 kV bus voltage, terminal voltage, angular speed, electrical torque and d–q axis stator current with and without the NAPC-supercapacitor modeling.

As shown in Fig. 6, the peak values of the 34.5 kV bus voltage of the test system and the output voltage of DFIG have risen. A shorter stabilization time was achieved with the NAPC-supercapacitor modeling and rotor EMF. In LVRT, the bus voltage of the test system with the positive and negative sequences, natural and forcing components and rotor EMF was at 0 p.u., and it was at 0.1 without them. With the intended LVRT model, the 34.5 kV bus bar voltage increased to 0.2 p.u., and the terminal voltage increased to 0.15 p.u. in case of a fault. When the NAPC-supercapacitor model is not used, the 34.5 kV bus bar voltage and terminal voltage became stable at 1.08 and 1.8 s, respectively, while with the intended LVRT model, the 34.5 kV bus bar voltage and terminal voltage became stable at 0.75 and 0.73 s, respectively. Using the NAPC-supercapacitor modeling and rotor EMF also reduced the oscillations in the angular speed, electrical torque and d–q axis stator currents, where in DFIG after a three-phase fault, they were stabilized using the positive and negative sequences, natural and forcing components and rotor EMF, at 2.5, 2.5, 6 and 5.35 s. Not using those, they were stabilized at about 6, 6, 6.5 and 6.5 s.

The oscillations during the three-phase fault were high when the NAPC-supercapacitor was not used. With the usage of the NAPC-supercapacitor, the oscillations in all parameters used in the three-phase fault occurring between 0.55 and 0.7 s were found to become stable in a short time. Examining the state of the oscillations occurring in the parameters in the three-phase fault, when the minimum and maximum intervals of the oscillations are examined,

terminal voltage was the most affected parameter, while the least affected one was angular speed.

Two-phase fault occurred in B 34.5 kV bus at 0.55–0.7 s. Figure 7 shows the comparison of the parameters with and without using the NAPC-supercapacitor modeling and rotor EMF on bus voltages.

For the two-phase fault, the bus voltage of 34.5 kV of the test system and the output voltage of DFIG were at about 0.3 p.u without using the NAPC-supercapacitor modeling and rotor EMF 0.5 p.u. while using them. With the LVRT model developed in the two-phase fault, the 34.5 kV bus bar voltage increased to 0.65 p.u. and the terminal voltage increased to 0.5 p.u. Not using the NAPC-supercapacitor model, the 34.5 kV bus bar voltage and terminal voltage became stable at 2.1 and 2.3 s, respectively, while with the developed LVRT model, the 34.5 kV bus bar voltage and terminal voltage became stable at 0.75 and 0.73 s, respectively. Same with the three-phase fault, using the positive and negative sequences, natural and forcing components and rotor EMF decreased the oscillations in the variations in angular speed, electrical torque and d–q axis stator current. The stabilization times of the variations following the two-phase fault in 34.5 kV bus with and without using the NAPC-supercapacitor modeling and rotor EMF were at 2.5, 2.5, 4.8, 4.8 s and 6, 6, 6.5, 6.5 s, respectively.

The oscillations during the two-phase fault were high when the NAPC-supercapacitor was not used. Using the NAPC-supercapacitor, the oscillations in all parameters used in the two-phase fault occurring between 0.55 and 0.7 s in the simulations were found to become stable in a short time. Examining the state of the oscillations occurring in the parameters in the two-phase fault, when the minimum and maximum intervals of the oscillations are examined, terminal voltage was the most affected parameter, while the least affected one was angular speed.

A one phase–ground fault was formed in B 34.5 kV bus at 0.55–0.7 s. Figure 8 shows the comparison of the parameters with and without using the NAPC-supercapacitor modeling and rotor EMF on bus voltages.

For this fault, the bus voltage of 34.5 kV of the test system and the output voltage of DFIG were at about 0.24 p.u without using the NAPC-supercapacitor modeling and rotor EMF and at 0.55 p.u. while using them. With the intended LVRT model, the 34.5 kV bus bar voltage increased to 34.5 p.u. and the terminal voltage increased to 0.55 p.u. in the phase–ground fault. Not using the NAPC-supercapacitor model, the 34.5 kV bus bar voltage and terminal voltage became stable at 1.3 and 1.4 s, respectively, while with the intended LVRT model, the 34.5 kV bus bar voltage and terminal voltage became stable at 0.75 and 0.73 s, respectively. Same with the three-phase fault, using the positive and negative sequences, natural and forcing components and rotor EMF decreased the oscillations in the variations in
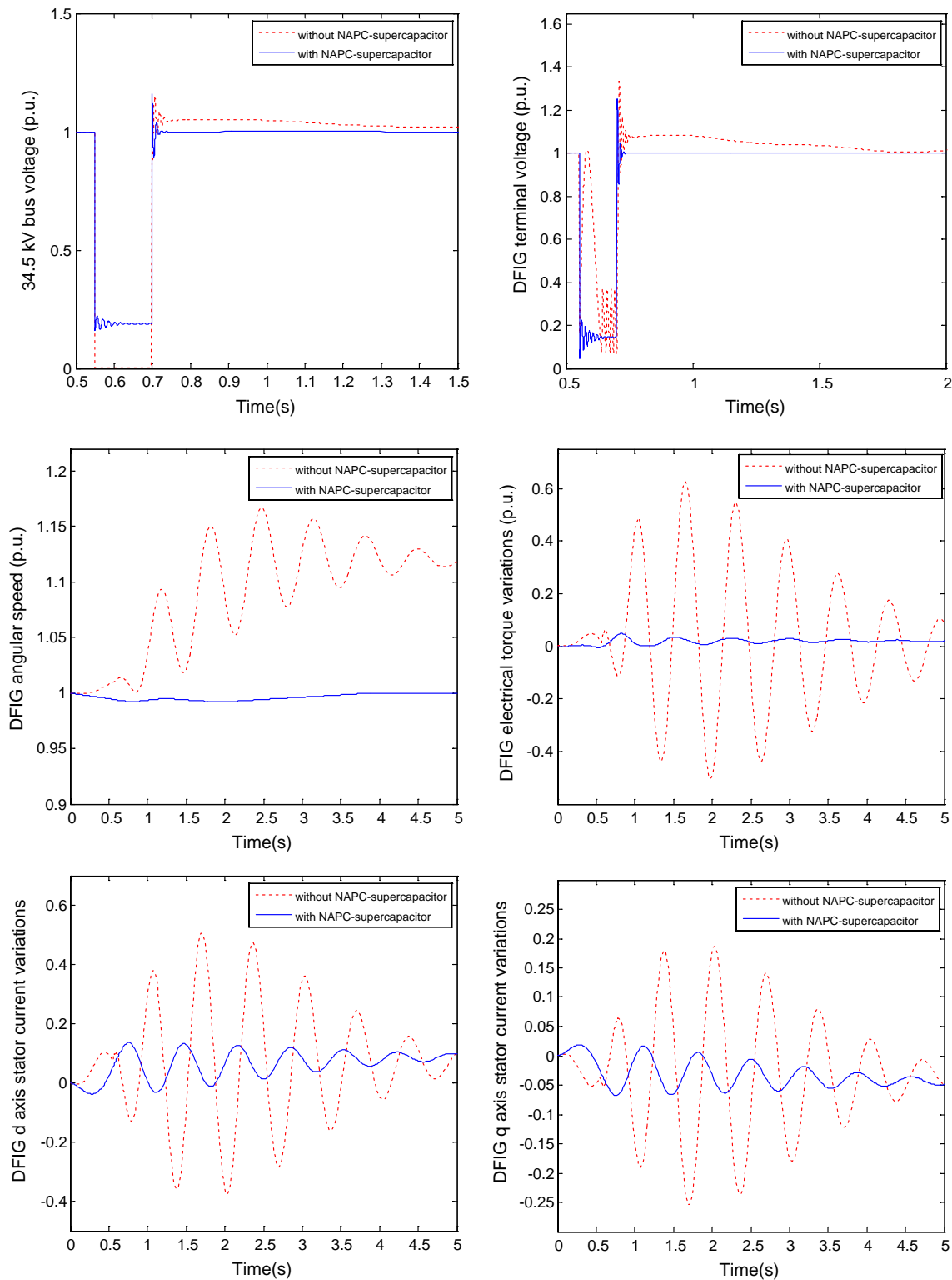
Fig. 6 System simulation results during three-phase fault

angular speed, electrical torque and d–q axis stator current. The stabilization times of the variations following the fault in 34.5 kV bus with and without using the

NAPC-supercapacitor modeling and rotor EMF were at 2.5, 2.5, 6.5, 6.5 s and 7.5, 7.5, 8, 8 s, respectively.

The oscillations in the phase–ground fault were high when the NAPC-supercapacitor was not used. Using the
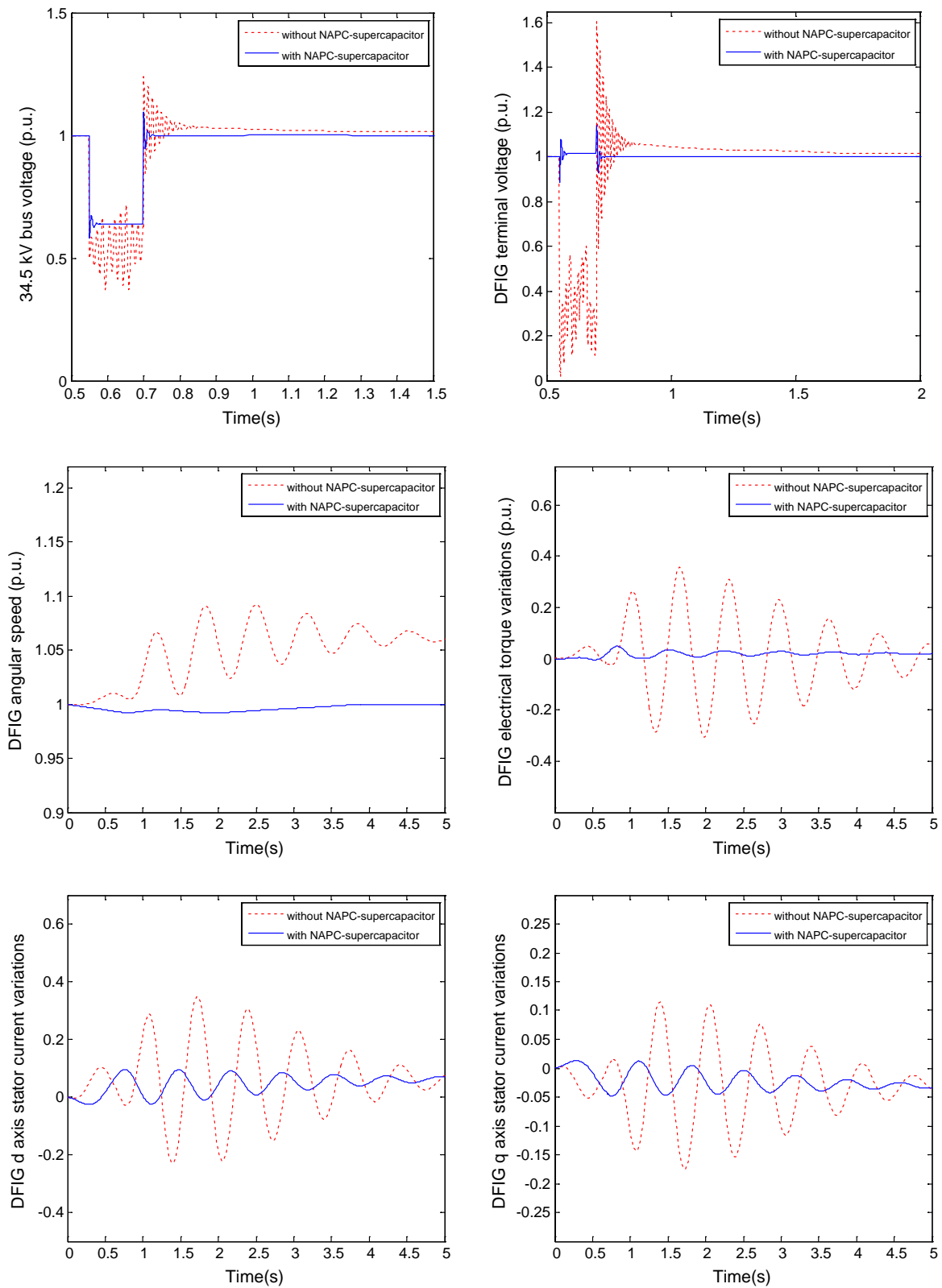
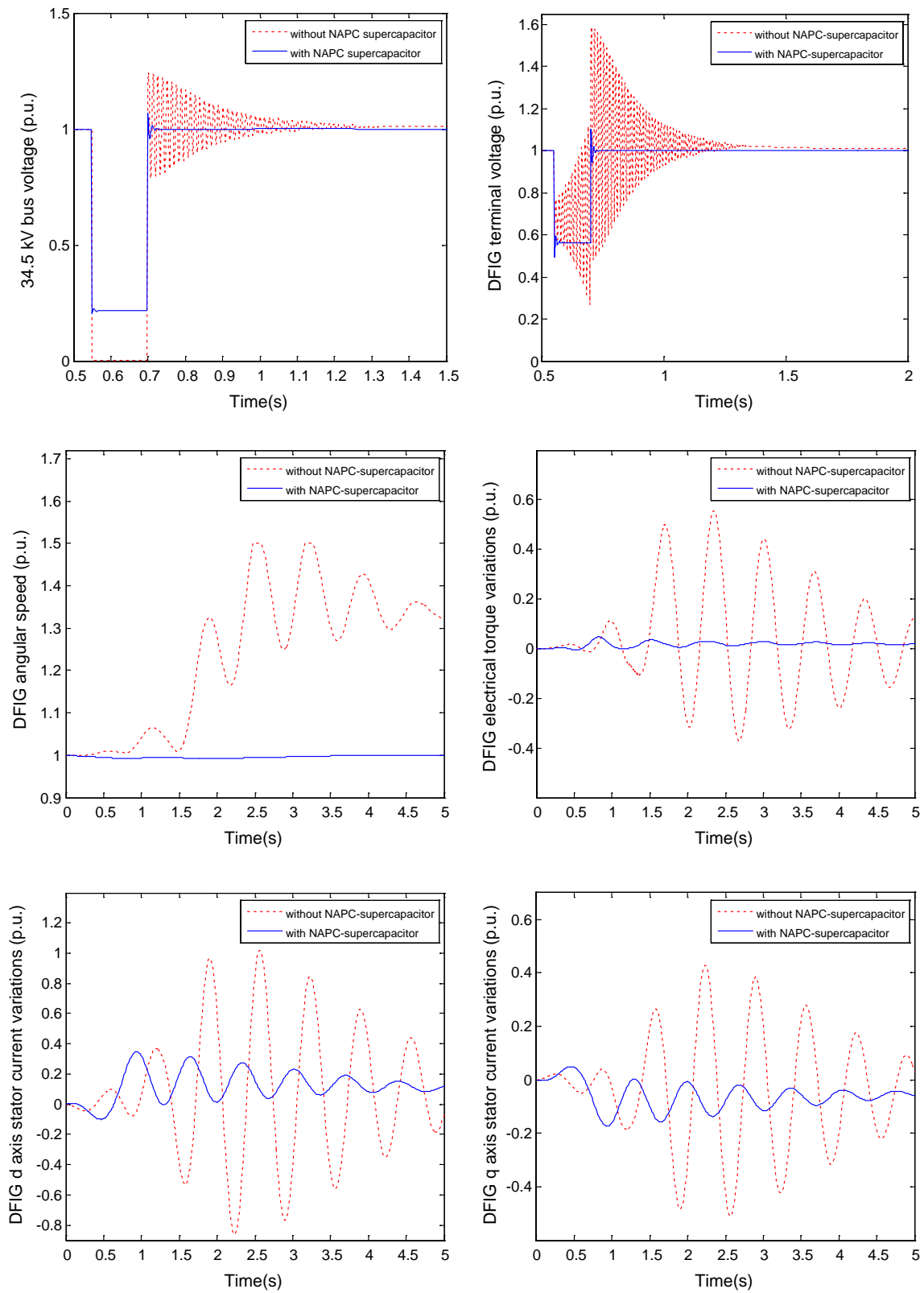**Fig. 7** System simulation results during two-phase fault

Fig. 8 System simulation results during a phase–ground fault

NAPC-supercapacitor, the oscillations in all parameters used in the phase–ground fault occurring between 0.55 and 0.7 s in the system were found to become stable in a short time. Examining the state of the oscillations occurring in the parameters in the phase–ground fault, when the minimum and maximum intervals of the oscillations are examined, terminal voltage was the most affected parameter, while the least affected one was q axis stator current.

6 Conclusion

For DFIG, there are theoretical methods for rotor-side converter and grid-side converter control against overvoltage and inrush current during balanced and unbalanced faults. In this study, we proposed an improved LVRT plan for DFIG consisting of a NAPC-supercapacitor modeling and a rotor EMF for balanced and unbalanced grid voltage dips. NAPC-supercapacitor modeling was successfully applied to solve the instability problems. We tested and compared the transient behaviors of the system in three-phase and two-phase faults with and without our proposed plan. In the three-phase fault in B 34.5 kV bus, decreases were observed in oscillations along with improved positive and negative sequences, natural and forcing components and rotor EMF in our proposed plan. In variation faults, we observed an increase in the terminal voltage of the DFIG. Examining the findings of the simulation exhibited that the post-transient fault oscillation damping occurred quite shortly with our proposed plan implemented to the wind turbine. The findings from the simulation system approve that the suggested LVRT plan is efficient in symmetrical and unsymmetrical grid voltage dips.

References

1. Tsili M, Papathanassiou S (2009) A review of grid code technical requirements for wind farms. IET Renew Power Gener 3(3):308–332
2. Petersson A, Thiringer T, Harnefors L, Petru T (2005) Modeling and experimental verification of grid interaction of a DFIG wind turbine. IEEE Trans Energy Convers 20(4):878–886
3. Muller S, Deicke M, De Doncker RW (2002) Doubly fed induction generator systems for wind turbines. IEEE Ind Appl Mag 8(3):26–33
4. Zhu R, Chen Z, Wu X, Deng F (2015) Virtual damping flux-based LVRT control for DFIG-based wind turbine. IEEE Trans Energy Convers 30(2):714–725
5. Kashkooli MA, Madani SM, Lipo TA (2019) Improved direct torque control for a DFIG under symmetrical voltage dip with transient flux damping. IEEE Trans Industr Electron. https://doi.org/10.1109/TIE.2019.2893856
6. Hu S, Lin X, Kang Y, Zou X (2011) An improved low-voltage ride-through control strategy of doubly fed induction generator during grid faults. IEEE Trans Power Electron 26(12):3653–3665
7. Yao J, Li H, Chen Z, Xia X, Chen X, Li Q, Liao Y (2013) Enhanced control of a DFIG-based wind-power generation system with series grid-side converter under unbalanced grid voltage conditions. IEEE Trans Power Electron 28(7):3167–3181
8. Mohseni M, Masoum MA, Islam SM (2011) Low and high voltage ride-through of DFIG wind turbines using hybrid current controlled converters. Electr Power Syst Res 81(7):1456–1465
9. Ebrahimkhani S (2016) Robust fractional order sliding mode control of doubly-fed induction generator (DFIG)-based wind turbines. ISA Trans 63:343–354
10. Xiong L, Li P, Wu F, Ma M, Khan MW, Wang J (2019) A coordinated high-order sliding mode control of DFIG wind turbine for power optimization and grid synchronization. Int J Electr Power Energy Syst 105:679–689
11. Alsmadi YM, Xu L, Blaabjerg F, Ortega AJP, Abdelaziz AY, Wang A, Albataineh Z (2018) Detailed investigation and performance improvement of the dynamic behavior of grid-connected DFIG-based wind turbines under LVRT conditions. IEEE Trans Ind Appl 54(5):4795–4812
12. Yang L, Xu Z, Ostergaard J, Dong ZY, Wong KP (2012) Advanced control strategy of DFIG wind turbines for power system fault ride through. IEEE Trans Power Syst 27(2):713–722
13. Li XM, Zhang XY, Lin ZW, Niu YG (2018) An improved flux magnitude and angle control with LVRT capability for DFIGs. IEEE Trans Power Syst 33(4):3845–3853
14. Xiao S, Geng H, Zhou H, Yang G (2013) Analysis of the control limit for rotor-side converter of doubly fed induction generator-based wind energy conversion system under various voltage dips. IET Renew Power Gener 7(1):71–81
15. Liang J, Qiao W, Harley RG (2010) Feed-forward transient current control for low-voltage ride-through enhancement of DFIG wind turbines. IEEE Trans Energy Convers 25(3):836–843
16. Liang J, Qiao W, Harley RG (2009) Direct transient control of wind turbine driven DFIG for low voltage ride-through. In: Power electronics and machines in wind applications. PEMWA 2009. IEEE, pp 1–7
17. Chondrogiannis S, Barnes M (2008) Stability of doubly-fed induction generator under stator voltage orientated vector control. IET Renew Power Gener 2(3):170–180
18. Liao K, Xu Y, Wang Y, Lin P (2019) Hybrid control of DFIGs for short-term and long-term frequency regulation support in power systems. IET Renew Power Gener 13(8):1271–1279
19. Liu Y, Jiang L, Smith JS, Wu QH (2018) Primary frequency control of DFIG-WTs using bang-bang phase angle controller. IET Gener Transm Distrib 12(11):2670–2678
20. Yan L, Chen X, Zhou X, Sun H, Jiang L (2018) Perturbation compensation-based non-linear adaptive control of ESS-DVR for the LVRT capability improvement of wind farms. IET Renew Power Gener 12(13):1500–1507
21. Döşoğlu MK (2017) Enhancement of SDRU and RCC for low voltage ride through capability in DFIG based wind farm. Electr Eng 99(2):673–683
22. Saeed MA, Khan HM, Ashraf A, Qureshi SA (2018) Analyzing effectiveness of LVRT techniques for DFIG wind turbine system and implementation of hybrid combination with control schemes. Renew Sustain Energy Rev 81:2487–2501
23. Qiao W, Venayagamoorthy GK, Harley RG (2009) Real-time implementation of a STATCOM on a wind farm equipped with doubly fed induction generators. IEEE Trans Ind Appl 45(1):98–107
24. Ananth DVN, Kumar GN (2016) Fault ride-through enhancement using an enhanced field oriented control technique for converters of grid connected DFIG and STATCOM for different types of faults. ISA Trans 62:2–18
25. Abbey C, Joos G (2007) Supercapacitor energy storage for wind energy applications. IEEE Trans Ind Appl 43(3):769–776

26. Jerin ARA, Kaliannan P, Subramaniam U, El Moursi MS (2018) Review on FRT solutions for improving transient stability in DFIG-WTs. IET Renew Power Gener 12(15):1786–1799

27. Döşoğlu MK (2016) Hybrid low voltage ride through enhancement for transient stability capability in wind farms. Int J Electr Power Energy Syst 78:655–662

28. Mohammadi J, Afsharnia S, Vaez-Zadeh S, Farhangi S (2016) Improved fault ride through strategy for doubly fed induction generator based wind turbines under both symmetrical and asymmetrical grid faults. IET Renew Power Gener 10(8):1114–1122

29. Döşoğlu MK, Güvenç U, Sönmez Y, Yılmaz C (2018) Enhancement of demagnetization control for low-voltage ride-through capability in DFIG-based wind farm. Electr Eng 100:491–498

30. Döşoğlu MK (2016) A new approach for low voltage ride through capability in DFIG based wind farm. Int J Electr Power Energy Syst 83:251–258

31. Döşoğlu MK, Arsoy AB, Güvenç U (2017) Application of STATCOM-supercapacitor for low-voltage ride-through capability in DFIG-based wind farm. Neural Comput Appl 28(9):2665–2674

32. Döşoğlu MK, Arsoy AB (2016) Transient modeling and analysis of a DFIG based wind farm with supercapacitor energy storage. Int J Electr Power Energy Syst 78:414–421

33. Wu F, Zhang XP, Godfrey K, Ju P (2007) Small signal stability analysis and optimal control of a wind turbine with doubly fed induction generator. IET Gener Transm Distrib 1(5):751–760

34. Krause PC (2002) Analysis of electric machinery, 2nd edn. McGraw-Hill, New York

35. Ekanayake JB, Holdsworth L, Jenkins N (2003) Comparison of 5th order and 3rd order machine models for double fed induction generators (DFIG) wind turbines. Electr Power Syst Res 67(3):207–215

36. Slootweg JG, Polinder H, Kling WL (2001) Dynamic modelling of a wind turbine with doubly fed induction generator. IEEE Power Eng Soc Summer Meet 1:644–649

37. Mohammadi J, Afsharnia S, Vaez-Zadeh S (2014) Efficient fault-ride-through control strategy of DFIG-based wind turbines during the grid faults. Energy Convers Manag 78:88–95

38. Mohammadi J, Afsharnia S, Ebrahimzadeh E, Blaabjerg F (2017) An enhanced LVRT scheme for DFIG-based WECSs under both balanced and unbalanced grid voltage sags. Electr Power Compon Syst 45(11):1242–1252

39. Gaiceanu M (2012) MATLAB/SIMULINK-based grid power inverter for renewable energy sources integration. In: MATLAB—a fundamental tool for scientific computing and engineering applications, pp 1–219

40. Rona B, Güler Ö (2015) Power system integration of wind farms and analysis of grid code requirements. Renew Sustain Energy Rev 49:100–107